PCCP

PAPER

View Article Online
View Journal | View Issue

Cite this: *Phys. Chem. Chem. Phys.*, 2023, **25**, 27417

# Element-ratio dependence of the 5d-states of Au and Pt in solid-solution-type Au–Pt alloy nanoparticles studied by X-ray absorption spectroscopy and density functional theory

Takeshi Morita, *[a] Shunki Ogawa,†[a] Tomotaka Kayama,†[a] Wataru Ono,[a] Shinya Tamura,[a] Kazuki Umeda,[a] Tsubasa Iwamatsu,[b] Nobuo Uehara[b] and Takehisa Konishi*[a]

Received 22nd June 2023,
Accepted 30th August 2023

DOI: 10.1039/d3cp02900j

rsc.li/pccp

Solid-solution-type Au–Pt alloy nanoparticles (NPs) were prepared from the nanoclusters of each metal using the polymer-conjugated fusion growth method. The elemental mapping analysis showed that the mixing state of the elements in the NPs drastically changed in the narrow reaction-temperature range from 100 °C to 180 °C. For their various mixing states, the 5d-states of Au and Pt atoms in the alloy NPs were investigated on the basis of the white line intensities of X-ray absorption near edge structure (XANES). Then, the 5d-states of Au and Pt atoms in a model crystalline ordered alloy structures were investigated on the basis of the theoretically calculated XANES spectra using density functional theory (DFT) in the whole composition range. The DFT calculation showed that the changes in the absorption spectra near the Pt and Au edges are caused by the change in the occupation of the Pt 5d-states and the orbital hybridisation of the Au 5d-states with the 5d-states of neighbouring Pt atoms around an Au atom, respectively.

## 1. Introduction

Nanoparticles (NPs) of single elements and alloys have been extensively investigated because of their unique potential in functional materials,[1,2] electrochemical applications[3,4] and optical devices.[5–8] The chemical activities of alloy NPs can be tuned by manipulating their electronic and geometric structures.[9–12] Solid-solution-type alloy NPs greatly vary in their electronic and geometric structures depending on the element hybridisation and mixing of constituent elements.[13–17] For gold (Au) and platinum (Pt) alloy NPs, Xiao *et al.* theoretically investigated the surface and size effects on the alloying ability and the phase stability of immiscible alloy NPs.[18] The study showed that the alloy is formed by the constituents of Au and Pt as the NPs against the immiscibility in the bulk phase behaviour. Solid-solution-type alloy NPs have been prepared using various techniques, such as laser irradiation,[19] ion sputtering,[20] arc plasma deposition,[21,22] co-impregnation,[23] microemulsion,[24] simultaneous reduction[25] and fusion growth.[26,27]

The reduction step of tetrachloroauric(III) acid ($[AuCl_4]^-$) is widely applied to the chemical synthesis processes of neat Au NPs.[28–30] In contrast, we have discovered a chemical synthesis method uniquely from Au nanoclusters (NCs) without the need for a reduction step during the NP formation.[31] In this method, the structural collapse of a thermoresponsive polymer *via* a random coil–globule transition is applied to the NP formation, hereafter referred to as the polymer-conjugated fusion growth method. Poly(*N*-isopropylacrylamide) (*p*-NIP)-conjugated Au NCs were effectively used in this method. Usón *et al.* have reported the spontaneous formation of Au–Pt alloyed NPs from small NPs (below 5 nm) of each metal.[26] This spontaneous formation proceeds through an ageing process of the small NPs, also without a reduction step, and takes 150 h. Recently, we have reported bimetallic Au–Pt NP synthesis from NCs of Au and Pt applying the polymer-conjugated fusion growth method.[27] It is expected that the mixing of neat NCs of various kinds of elements would create alloy NPs composed of the elements of the different NCs. From this viewpoint, this synthesis approach has a wide potential in the hybridisation of elements.

In general, the hybridisation of elements in alloy NPs leads to two main types of effects for the specific activity: the electronic and geometric contributions.[32,33] The hybridised component exerts an electronic influence on the NPs, resulting

---

[a] *Department of Chemistry, Graduate School of Science, Chiba University, Chiba 263-8522, Japan. E-mail: moritat@faculty.chiba-u.jp, konishi@faculty.chiba-u.jp*

[b] *Graduate School of Engineering, Utsunomiya University, Utsunomiya Tochigi 321-8585, Japan. E-mail: ueharan@cc.utsunomiya-u.ac.jp*

† SO and TK contributed equally to this work.

in a change in electron density and charge, which in turn causes enhancement of the activity. For the geometric effect, in the case that both the NPs and the hybridised component act as reaction catalysts, these multiple components are adjacent to each other and can interact with a substrate simultaneously, resulting in higher catalytic activity. The electronic and geometric effects can occur in the solid-solution-type alloy NPs. In addition, solid solutions have been reported to have properties of the intermediate range of each element on the periodic table of the alloying elements.[34,35] Therefore, insights into the electronic structure of the constituent elements in solid-solution-type alloy NPs are vital to understanding the core mechanism of the specific activity of the alloyed NPs.

The X-ray absorption fine structure (XAFS) is one of the most effective methods for the investigation of the electronic structure. The white line of the Pt $L_3$ X-ray absorption near edge structure (XANES) corresponds to the Pt $2p_{3/2}$ orbital → 5d orbital transition. The intensity of this white line reflects the number of unoccupied Pt 5d-states, which can be utilised as a fingerprint of the oxidation states.[36,37] Similarly, the white line of the Au $L_3$ XANES spectra, when present as in trivalent Au compounds, corresponds to the Au $2p_{3/2}$ orbital → 5d orbital transition, reflecting the number of unoccupied Au 5d-states. Wang *et al.* have reported on the electronic behaviour of Au–Pt alloys using the $L_{3,2}$-edge XANES measurement and the density functional theory (DFT) calculation.[38] The study found that the Au and Pt element diluted in Pt and Au (Au : Pt = 1 : 9 or Pt : Au = 1 : 9) shows Pt-like and Au-like electronic structure, respectively. Sham *et al.* have reported the $L_{3,2}$-edge white line anomaly in the Au–Pt nanowire.[39] Piotrowski *et al.* have reported the theoretical calculation on the electronic structure of Pt-based nanoalloys (including $Pt_nAu_{55-n}$ alloy) with the core–shell structure.[40] The study revealed the mechanism of the chemical reaction activity in terms of the total energy and the centre of gravity of the occupied Pt d-state as a function of the composition ratio.

Therefore, to address this pressing current problem in understanding and controlling the chemical activities in the solid-solution-type NP alloys, we must clarify the electronic structure changes by elemental mixing in terms of occupational change and orbital hybridisation. Here, the 5d-states of Au and Pt elements in the solid-solution-type Au–Pt alloy NPs were investigated on the basis of the $L_3$ XANES spectra. The alloyed NPs were synthesised using the polymer-conjugated fusion growth method under hydrothermal conditions from 100 °C to 220 °C. The utilisation of the nanomaterials enables us to clarify the change in electronic structure in the solid solution process of the constituent elements because the mixing state of the elements in the present NP synthesis drastically changed with a slight rise in reaction temperatures. For a quantitative understanding of the relationship between the occupation of the 5d-states and the intensity of the white line in XANES spectra, the 5d-states of Au and Pt atoms in a model crystalline ordered alloy structures are investigated on the basis of theoretically calculated XANES spectra. The calculation provides theoretical reference XANES spectra of Au–Pt alloys for which bulk standard samples cannot be easily obtained over the whole compositional range. In addition, we discuss changes in the real space charge distribution around the Au and Pt atoms upon alloy formation on the basis of the calculation.

# 2. Experimental

## 2.1 Preparation of Au NCs

All glassware used in the NC synthesis was cleaned with aqua regia (three parts HCl and one part $HNO_3$), rinsed in deionised water and ultrapure water, and dried in an oven prior to use. Aqueous 0.10 wt% tetrachloroauric acid ($HAuCl_4$) solution was prepared with 0.0514 g $HAuCl_4$–$4H_2O$ (Fujifilm Wako Pure Chemicals Co., 99.0%) and 50 mL ultrapure water using a volumetric flask. Aqueous 1.00 wt% tetraethylene glycol solution was prepared with 0.500 g tetraethylene glycol, adding ultrapure water to a total weight of 50.000 g. The mixture of 10 mL of the 0.10 wt% $HAuCl_4$ solution and 50 mL of the 1.00 wt% tetraethylene glycol solution was adjusted to pH = 2.5 using 1 mol $L^{-1}$ hydrochloric acid, followed by adding ultrapure water to a total volume of 100 mL. Aqueous 0.1 mol $L^{-1}$ sodium borohydride ($NaBH_4$) solution was prepared with 0.0378 g $NaBH_4$–$4H_2O$ (Kanto Chemical Co., Inc., Atomic Absorption Spectrometry) and a 10 mL volumetric flask. The $NaBH_4$ solution of 1.0 mL was added to the mixture of $HAuCl_4$ solution and tetraethylene glycol solution in 5 divided 0.2 mL portions. The reaction solution was kept at 25 °C for 6 h under stirring. The resultant solution, both Au NCs and Au NPs, was passed through a silica-gel column to remove by-products, such as NPs with an extinction band around 520 nm, and a solution containing only NCs with diameters of less than 2 nm was prepared. The other procedures have been described in our previous papers.[31,41]

## 2.2 Preparation of Pt NCs

All glassware used in the NC synthesis was cleaned with aqua regia (three parts HCl and one part $HNO_3$), rinsed in deionised water and ultrapure water, and dried in an oven prior to use. The Pt NC synthesis was performed with modification for this study on the basis of the procedure reported in the literature.[42] Aqueous 1 g-Pt $L^{-1}$ ($5.142 \times 10^{-3}$ mol $L^{-1}$) hexachloroplatinic acid $H_2PtCl_6$ was prepared by 0.7993 g hydrogen hexachloroplatinate(IV) hexahydrate $H_2Cl_6Pt$–$6H_2O$ (Koso Chemical Co., Ltd., special grade reagent) and ultrapure water using a 3 mL volumetric flask. Aqueous 8.00 wt% trisodium citrate solution was prepared by 8.00 g trisodium citrate dihydrate (Kanto Chemical Co., Inc., 99.0%) and ultrapure water to a total weight of 100.0 g. The prepared 8.00 wt% trisodium citrate solution was successively diluted to prepare trisodium citrate solutions of 4.00 wt%, 2.00 wt% and 1.00 wt% to synthesise the Pt NCs with various sizes. Ultrapure water (240 mL) was prepared in a round-bottom flask, followed by boiling using a mantle heater under a nitrogen gas purge for 1 h. The prepared $H_2PtCl_6$ solution of 15 mL was added to the flask, followed by boiling the solution for 5 min. The prepared trisodium citrate solution of 30 mL was added to start the NC formation. The duration time of the reaction was set to 2 h, followed by cooling using storage in ice.

### 2.3 Synthesis of *p*-NIP

The *p*-NIP used was synthesised from the corresponding monomer *via* a radical polymerisation method reported elsewhere.[43] In brief, 19.24 g (0.17 mol) of isopropylacrylamide, 0.35 mL of 3-mercaptopropionic acid and 0.82 g of azobisisobutyronitrile added into a 500 mL round-bottom separable flask equipped with a condenser were dissolved with 70 mL of methanol. The mixture was maintained at 60 °C for 4 h under a nitrogen atmosphere. The resultant solution was poured into the same volume of cooled diethyl ether. The crude precipitate was purified with methanol and diethyl ether. The purified precipitate was dissolved in water and freeze-dried. The molecular weight of *p*-NIP and the dispersion were adjusted by careful screening and optimised for the present fusion growth.

### 2.4 Protocol for Au–Pt alloy formation

The hydrothermal reaction of the alloys was performed using a high-temperature and high-pressure vessel with an observation window. The vessel was made of titanium to operate the reaction because titanium has a relatively low thermal expansion coefficient and high chemical resistance. The sample temperature was monitored using a J-type thermocouple. A pressure of up to 5 MPa, which prevents the boiling of the aqueous solutions at temperatures above 100 °C, was applied during the reaction. The hydrothermal reaction temperatures were set at 100 °C, 120 °C, 140 °C, 160 °C, 180 °C, 200 °C and 220 °C. The reaction time was set at 1 h, followed by cooling using storage in ice. The concentration of the aqueous *p*-NIP solution was adjusted to be 0.10 wt% after the concentration optimisation. The 0.10 wt% *p*-NIP solution, the Au NC solution and the Pt NC solution were added into a 4 mL glass bottle to be set at a volume ratio of 20 : 9 : 3 for the reactions at all temperatures, respectively.

### 2.5 Electron microscopy

The following methods were applied to the product analysis: transmission electron microscopy (TEM) for observing the structural aspects, scanning TEM (STEM) in both the bright-field (BF) and high-angle annular dark field (HAADF) modes for the local analysis of the NPs, energy-dispersive X-ray spectrometry (EDS) for estimating the element ratio and elemental mapping using STEM-EDS analysis.

TEM grids were prepared by placing drops of the solutions on carbon-coated grids and drying them at room temperature for one day. TEM images were obtained using a field-emission-type electron microscope (JEOL, JEM-2100F) under an acceleration voltage of 120 kV and using an ultrahigh-resolution charge-coupled device (CCD) camera (GATAN, UltraScan 1000).

HAADF-STEM images and elemental mapping of the products synthesised at 100 °C, 140 °C and 180 °C were obtained using a transmission electron microscope (JEOL, JEM-ARM200F) and an energy-dispersive X-ray spectrometer (JEOL, JED-2300T DrySDD100 mm). The acceleration voltage, the magnification and the number of pixels were set at 200 kV, $4 \times 10^6$ and 256 × 256, respectively. During the analysis, the spot size was set at 5C mode, around 1 Å in electron beam diameter at the sample position.

### 2.6 XANES

The Pt $L_3$ edge XANES spectra were acquired at the beamline BL11 of SAGA Light Source, Japan.[44] The XANES signals of the prepared alloy were acquired in the fluorescence mode. A silicon drift detector was placed near the sample container during the fluorescence XANES measurements. The spectra were recorded in the quick scan mode. For measuring the standard sample, the XANES signals were obtained in the transmission mode using foils of Au or Pt. The XANES data were analysed using the Athena software.[45]

The Au $L_3$ edge XANES spectra were measured at the BL-12C of the Photon Factory (PF) at the High-Energy Accelerator Research Organization (KEK), Tsukuba, Japan.[46] The XANES signals of the prepared alloy were acquired in the fluorescence mode. A silicon drift detector was placed near the sample container during the fluorescence XANES measurements. The spectra were acquired in the step-scan mode. For measuring the standard sample, the XANES signals were obtained in the transmission mode using foils of Au or Pt. The XANES data were analysed using the Athena software.[45]

## 3. Theoretical calculations

In order to obtain insight into the electronic structure probed by XANES spectroscopy, we calculated the electron density, the density of state (DOS) and the XANES of pure Au, Pt and model Au–Pt bulk-ordered alloys based on DFT using first-principles electronic structure code WIEN2k[47] with the OPTIC package.[48] Calculations have been performed in the all-electron scheme with the full-potential (linearised) augmented plane-wave ((L)APW) + local orbital (lo) method, including relativistic effects.[49] PBE-GGA[50] is employed for the exchange–correlation potential. The calculations were carried out neglecting the core hole effects, which, in the case of metals, do not drastically alter the overall spectral features. In the XANES calculations, we added to the basis set high-lying Local Orbitals with *d*-symmetry for a better description of the higher energy side of the spectra.

In this report, we present calculations on the face-centred cubic (fcc) $L1_0$ and $L1_2$ type bulk ordered alloys along with the elemental metals. These structures exhaust all the fcc-type binary structures with the 1 × 1 × 1 unit cell. The structural models used for the calculations are displayed in Fig. 1. Ideal fcc atomic positions with lattice constants estimated by Vegard's law were adopted in the calculation. The calculation was performed assuming linear polarised X-ray. The calculated spectra were averaged over polarisation directions. Table 1 shows the structural parameters used in the calculation. We set $R_{\mathrm{mt}}$ (muffin-tin radius) as 2.50 bohr and $RK_{\max}$

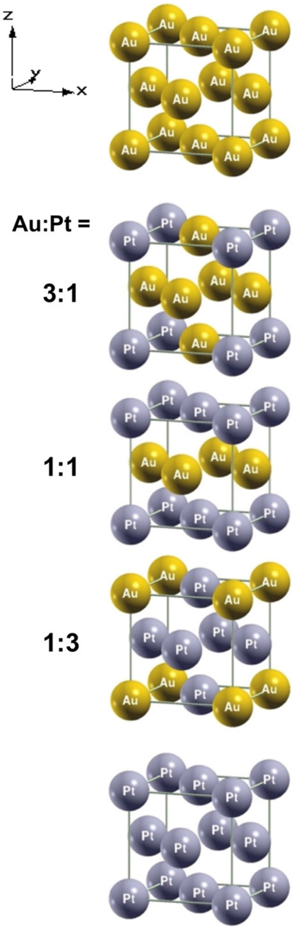

Fig. 1 Model structures used for the present DFT calculation. From the top to the bottom, neat Au, Au–Pt alloys and neat Pt.

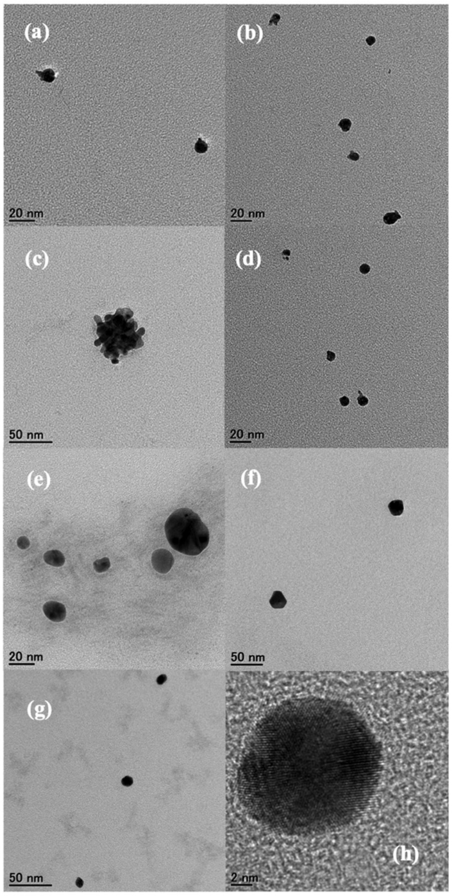

Fig. 2 BF-TEM images of the synthesised Au–Pt alloy NPs using the thermoresponsive-polymer-conjugated fusion growth method. (a) 100 °C, (b) 120 °C, (c) 140 °C, (d) 160 °C, (e) 180 °C, (f) 200 °C and (g) 220 °C. The TEM image of (h) shows an enlarged image of the typical NP synthesised at 220 °C for crystallinity evaluation.

(the plane wave cutoff) as 10.0. Neat Au and neat Pt were calculated with a *k*-mesh of 30 000 points in the first Brillouin zone.

## 4. Results and discussion

### 4.1 NP morphology by TEM

Fig. 2 shows TEM images of the products synthesised at temperatures ranging from 100 °C to 220 °C. As the reaction temperature increased, the morphology aspects in the products gradually changed and are summarised as follows. The complex structure composed of the central core NPs and the smaller particles located on the core NP surface was produced at 100 °C and 120 °C. The inhomogeneity of the particle morphology seemed to be slightly reduced at 120 °C. Aggregates composed of the small particles were identified specifically at 140 °C. The complex structure of the central core NPs and the smaller particles observed at 100 °C and 120 °C was also produced at 160 °C. Spherical NPs with smooth surfaces were synthesised at 180 °C. At 200 °C and 220 °C, the further increase in reaction temperature led to little change in the NP morphology compared with that of the NPs synthesised at 180 °C. The morphology of the NPs synthesised at 200 °C and 220 °C was analogous to that of the NPs formed at 180 °C. In addition, as shown in Fig. 2(h), although the fusion growth method is classified as a coalescence process,[51] the present fusion growth produced alloy NPs with high crystallinity rather than multiple-domain NPs.

Neat Au NPs have been fabricated using the thermoresponsive-polymer-conjugated fusion growth method below 90 °C.[31,41] The present temperature dependence shown in Fig. 2 indicates that the reactant solutions for alloy formation were subjected to hydrothermal treatment temperatures up to 180 °C. The hydrothermal treatment caused the reactant NCs to overcome the miscibility gap shown in the phase diagram and

Table 1 Structural parameters used in the calculations

| Composition ratio | The number of atoms in the unit cell | Lattice constant [Å] |
|---|---|---|
| Neat Au | 1 | 4.0783 |
| Au : Pt = 3 : 1 | 4 | 4.0397 |
| Au : Pt = 1 : 1 | 2 | $a = b = 2.8293$, $c = 4.0012$ |
| Au : Pt = 1 : 3 | 4 | 3.9626 |
| Neat Pt | 1 | 3.9240 |

the differences in the cohesive energy of crystal formation between Au and Pt.[52–54] In this viewpoint, the application of the higher temperature has an advantage for the hydrothermal NP formation. However, the relatively lower dispersion of the products was observed in the synthesis performed at 225 °C, resulting in aggregation and sedimentation of the synthesised NPs about two weeks after the reaction was performed. The present reaction was conducted under hydrothermal conditions. The polymer material *p*-NIP was applied to the fusion growth method. In addition, it is known that water at elevated temperatures has high activity due to the increase in the value of the ion product of water, $K_W$, to increase the concentrations of hydrogen and hydroxide ions.[55,56] The hydrothermal condition could affect the polymer material due to the so-called subcritical water with high activity. Considering these issues, the optimum temperature was determined to be 180 °C in the present reaction conditions.

### 4.2 Elemental mapping

Fig. 3 shows the HAADF-TEM image and the elemental mapping of the prepared Au–Pt alloy NPs synthesised at 100 °C, 140 °C and 180 °C. As shown in Fig. 3, the products prepared at 100 °C have the central core NP composed almost entirely of Au element and the smaller particles composed of Pt element. The composition ratio of the NP formed at 100 °C was estimated to be Au : Pt = 24 : 1 using STEM-EDS analysis, indicating that the application of reaction temperature of 100 °C did not lead to a solid solution. At 140 °C, the elemental mapping indicated that the observed aggregate was composed of small particles separately composing both Au and Pt. As shown in Fig. 3, a hydrothermal reaction temperature of 180 °C provided sufficient element mixing in the NPs, which led to the formation of a solid-solution-type alloy. The elemental ratio was determined to be Au : Pt = 2.3 : 1. The homogeneity degree of the solid solution of the Au–Pt alloy NPs was clearly improved compared with that reported in our previous study.[27] The synthesis refinement was mainly caused by the optimisation of Pt NC size, which was adjusted by controlling the citric acid concentration, as described in Section 2.2. The optimum citric acid concentration in the present experimental condition was determined to be 2.00 wt%, resulting in 2.05 nm in diameter of Pt NC size.

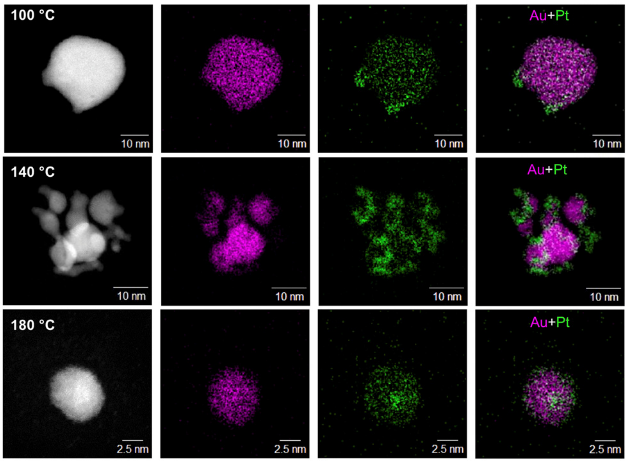

Fig. 3 HAADF-STEM images (left-hand side images) and elemental mapping of Au–Pt alloy NPs synthesised at 100 °C, 140 °C and 180 °C. Au and Pt are represented by pink and green coloured dots, respectively.

Ishimoto and Koyama found that the mechanism of the specific solid solution in nanomaterials is employed by the enlarged entropic contribution in nanosize, compared to the bulk materials.[57] The following formation process is proposed in the present synthesis: (1) randomly gathering the Au and Pt NCs *via* the random coil–globule transition of the thermoresponsive polymer, (2) thermodynamically assisting the fusion growth of Au and Pt NCs with each other by the hydrothermal treatment up to 180 °C and (3) stabilisation of the synthesised solid-solution-type NPs due to the enhanced entropic contribution in nanosize materials.

In general, fusion growth is classified as a coalescence formation process, resulting in the formation of NP with multiple domains, compared to the Ostwald ripening growth process.[51,58] However, as shown in Fig. 2(h), the products synthesised by the present fusion growth had high crystallinity. The morphologies and elemental mapping shown in Fig. 2 and 3 indicate that a

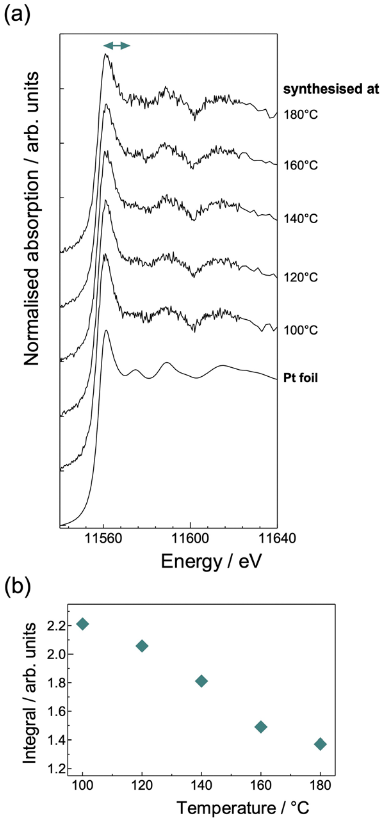

Fig. 4 (a) Pt $L_3$ XANES spectra for Au–Pt alloy NPs synthesised using the polymer-conjugated fusion growth. The XANES spectrum for Pt foil is also shown as a standard sample of Pt metal. (b) Temperature dependence of integrals of the white line in the Pt $L_3$ XANES spectra of the Au–Pt alloy NPs. Integrals were calculated using the energy region of the XANES profile from 11561 to 11573 eV indicated by the green arrow in (a).

temperature rise led to wide variations in the elemental mixing from 100 °C to 180 °C. The mixing state of Au and Pt elements in the particles significantly changed even in the narrow temperature range from 100 °C to 180 °C. On these bases, investigations on the products synthesised from 100 °C to 180 °C should extract the electronic structure changes of alloy NPs in a wide composition range of Au and Pt element ratios.

### 4.3 Temperature dependence of XANES spectra

For NPs with widely various mixing states of elements, the electronic state (the occupation) of the 5d-states was clarified on the basis of the integrals of the white line in XANES signals. Fig. 4(a) shows the Pt $L_3$ XANES signals for the Au–Pt alloy NPs synthesised by the present fusion growth method. As shown in Fig. 4(a), the peak height of the white line in the XANES spectra decreased as the reaction temperature increased. A decrease in the peak height means an increase in the number of electrons in the Pt 5d-states, as described in Introduction. Fig. 4(b) shows the integrals of the peak portion of the white line in the XANES spectra as a function of the reaction temperature. As shown in Fig. 4(b), the integrals gradually decreased with increasing the reaction temperature. The temperature dependence is evidence that the elemental mixing of Au and Pt through the fusion growth led to the change in the number of electrons in Pt 5d-states. The change in the integrals shown in Fig. 4(b) corresponds to the results by NP morphology shown in Fig. 2 and the temperature dependence of the mixing state shown in Fig. 3.

Fig. 5(a) shows Au $L_3$ XANES signals for the Au–Pt alloy NPs synthesised using the fusion growth method. Fig. 5(b) shows the overlapped profiles shown in Fig. 5(a) for spectral comparison. As discussed in Fig. 4, the elemental mixing of Au and Pt through the fusion growth led to an increase in the number of electrons in the Pt 5d-states. However, as shown in Fig. 5(b), little change in the Au $L_3$ edge was identified for the alloy NPs with the maximum Pt ratio of Au : Pt = 2.3 : 1 studied here. This is discussed in detail later in the whole composition range using the DFT calculations for Au–Pt alloys.

### 4.4 DFT calculation of the electronic state in the crystal model

The relationship between integrals of XANES signals and the occupation of the 5d states in the Au–Pt alloy lattice models was investigated using DFT calculation. The calculated results are shown in Fig. 6–8. The occupation numbers of the 5d states shown in the figures are defined as the integral of the d-projected DOS within the muffin-tin sphere around each atomic species and are dependent on the choice of the muffin-tin radii. The size of the muffin-tin spheres in the calculation is depicted

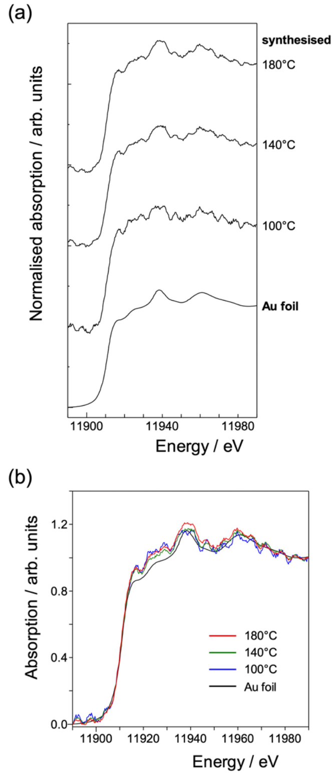

Fig. 5 (a) Au $L_3$ XANES spectra for Au–Pt alloy NPs synthesised at 100 °C, 140 °C and 180 °C. The XANES signal for Au foil is also shown as a standard sample of Au metal. (b) Overlapped Au $L_3$ XANES spectra for Au foil and Au–Pt alloy NPs synthesised at 100 °C, 140 °C and 180 °C. For quantitative comparison, background was subtracted for the XANES spectra shown in (a).

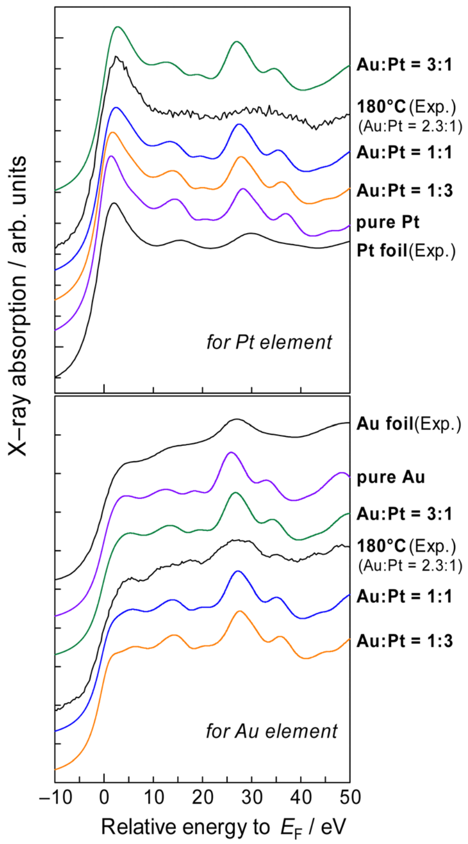

Fig. 6 XANES obtained from the DFT calculation for the crystal models shown in Fig. 1 with Au : Pt = 1 : 0, 3 : 1, 1 : 1 and 1 : 3. The XANES spectra of alloy NPs synthesised at 180 °C are also shown to compare the theoretical and experimental results. "Exp." in parentheses indicates the experimentally measured data of XANES.

in Fig. 9. A correlation between integrated X-ray absorption spectra and the number of empty states in the 5d-states was found for both Au and Pt edges, *i.e.*, an increase in the XANES intensity near the $L_3$ edge corresponds to a decrease in the number of electrons in the 5d-states.

Fig. 6 shows XANES calculated using the DFT theory and the alloy model described in Theoretical Calculations. The experimental XANES spectra of Au–Pt alloy NPs synthesised at 180 °C are also shown for comparison with the theoretically calculated data. The elemental ratio of the synthesised NPs was estimated to be Au : Pt = 2.3 : 1 using the STEM and EDS analyses. As shown in Fig. 6, the calculated spectra show reasonable agreement with the experimental spectra of the standard foil sample in terms of the spectrum profile and the peak positions. The calculated spectral profiles in the near-edge region are also consistent with those of synthesised NPs.

Fig. 7 shows the XANES and the DOS of the Au–Pt alloy models. As shown in Fig. 7(a), the absorption intensities near the Pt edge were increased with increasing the Pt composition ratio to Au. The intensity increase is caused by an increase of unoccupied Pt 5d-states that can be seen from the unoccupied part of the d-projected DOS in the lower panel of Fig. 7(a). As shown in Fig. 7(b), the absorption intensities in XANES near the Au edge were also increased with increasing the Pt ratio. It can be seen from the lower panels of Fig. 7(a) and 7(b) that the absorption increase is caused by the orbital hybridisation of Au 5d-states with 5d-states of neighbouring Pt atoms.

Fig. 8 shows the integrals of the edge region of XANES spectra of Au and Pt as a function of the number of holes in the 5d-states. Changes in the occupation of 6s-, 6p-states and the number of electrons in the outside of the muffin-tin spheres also take place, which do not have a major effect on the white-line intensities. As discussed in Fig. 4, the occupation of the Pt 5d-states in the alloy NPs gradually increased with the proceeding elemental mixing between Au and Pt, which corresponded to an increase in the reaction temperature. As shown in Fig. 5, for Au, little change in the white line in the XANES was observed for the synthesised alloy NPs. Although the experimental composition ratio was limited to Au : Pt = 2.3 : 1 due to synthesis technique limitation under the present stage, the element-ratio dependence of the Au and Pt 5d-states was investigated using the present DFT calculation for Au–Pt alloys with the whole composition ranges of Au : Pt = 1 : 0, 3 : 1, 1 : 1, 1 : 3 and 0 : 1. As shown in Fig. 8(a), the integrals of the white line in XANES for Pt gradually increased with increasing Pt ratio, as observed in the experimental XANES. As shown in Fig. 8(b), the change in XANES for Au was rarely observed for the composition change from pure Au (Au : Pt = 1 : 0) to Au : Pt = 3 : 1, similar to the experimental result for the synthesised alloy

(a) for Pt element

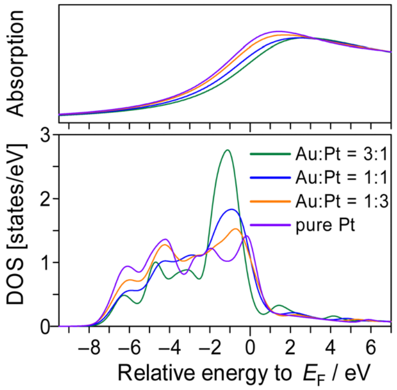

(b) for Au element

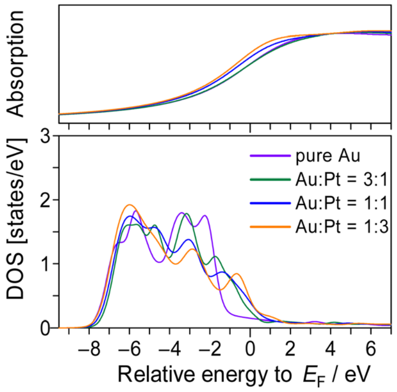

Fig. 7 (a) XANES and d-projected DOS for Pt from the DFT calculation using the crystal models shown in Fig. 1 with Au : Pt = 0 : 1, 1 : 3, 1 : 1 and 3 : 1. (b) XANES and d-projected DOS for Au from the DFT calculation using the crystal models shown in Fig. 1 with Au : Pt = 0 : 1, 1 : 3, 1 : 1 and 3 : 1. $E_F$ shown in the horizontal axes represents the Fermi level.

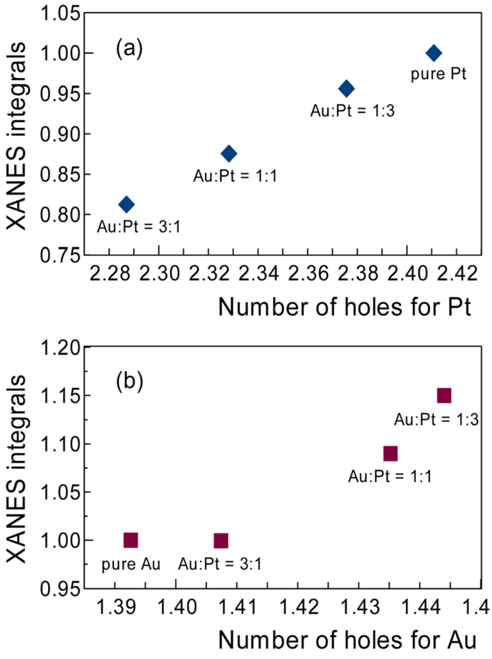

Fig. 8 Integrals of the edge region of the XANES spectra as a function of the number of holes in the 5d-states for (a) Pt and (b) Au. The number of holes is defined as the difference in the number of electrons from 10. The energy regions from −9.4 to 2.0 eV for Au and −9.4 to 3.0 eV for Pt in the XANES were used for the integration of the XANES spectra. The energy region from −9.4 to 0 eV for Au and Pt in the d-projected DOS was used for the estimation of the number of electrons in the 5d-states.

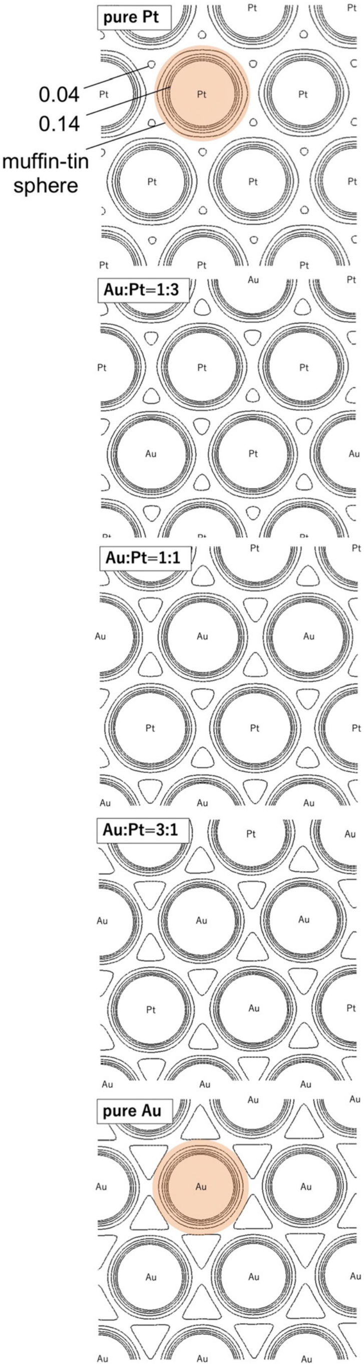

Fig. 9 Calculated electron densities for Au–Pt alloys. (from top to bottom) Pure Pt, Au : Pt = 1 : 3, Au : Pt = 1 : 1, Au : Pt = 3 : 1 and pure Au. The maximum and minimum contour values were 0.14 and 0.04 bohr$^{-3}$, respectively. The shadowed areas represent the muffin-tin sphere for each atomic species within which the number of electrons was counted (see text).

with the ratio of Au : Pt = 2.3 : 1. The integrals of the white line of XANES for Au element sharply increased with further increases in the Pt ratio. The present theoretical calculation showed that the changes in the edge region of the XANES spectra were caused by the following mechanism: the change of the occupation of the Pt 5d-states for the change in Pt $L_3$ and the orbital hybridisation of the Au 5d-states with the 5d-states of the neighbouring Pt atoms in the case of Au, where the 5d-states are well below the Fermi level ($E_F$) in the elemental metal.

### 4.5 DFT calculation of the electron density in the model alloys

We turn to changes in the real space charge distribution corresponding to the changes in the DOS and XANES spectra upon alloying. Fig. 9 shows the electron density in the (111) plane for each composition. In elemental Au, the electron density around each Au atom was almost spherical, reflecting the filled 5d states. With increasing Pt in the alloy composition, the electron distribution around the Au atoms deviated from the spherical shape, extending to neighbouring Pt atoms. For the Pt atoms, the distribution in the pure Pt was hexagon-shaped in the (111) plane, reflecting partially filled 5d-states in Pt. When the Au composition was increased, the nonspherical electron distribution became less pronounced. These results indicated that the atoms in the alloys were indeed intermediate between those of Au and Pt with respect to the interatomic chemical bonding.

## 5. Conclusions

The element-ratio dependence of the 5d-states of Au and Pt in the solid-solution-type alloy NPs was investigated on the basis of experimental $L_3$ XANES spectra and DFT calculations. The changes in the white line intensities of the $L_3$ XANES spectra clearly showed that the occupation of the Pt 5d-states in the alloy NPs gradually increased as the elemental mixing progressed under the higher reaction temperature. The present DFT investigation demonstrated that the occupation of the 5d-states in the Au atom decreased specifically above the Pt ratio of Au : Pt = 1 : 1, which was an opposite trend to the increase in the electron occupation of the Pt 5d-states. This result is evidence of the formation of intermediate electronic structures between the constituent elements of Pt and Au. The mechanism of the formation of the intermediate electronic structures in Pt and Au was clarified as the occupation change in the Pt 5d-states and the orbital hybridisation of the Au 5d-states with 5d-states of the neighbouring Pt atoms around the Au atom, respectively.

## Author contributions

The manuscript was written through the contributions of all authors. All authors approved to the final version of the manuscript.

## Conflicts of interest

There are no conflicts to declare.

## Acknowledgements

We are grateful to SAGA Light Source for providing the opportunity for the XAFS measurements (proposal no. 1911098F) and for the very kind experimental support. We express thanks to PF at KEK for the opportunity to perform the XANES measurements (proposal no. 2018G544, 2020G644). We express our appreciation to Dr Mari Morita and Mr Kazuhiko Moriyama for the detailed analyses of the elemental mapping of the nanoparticles supported by the Nanotechnology Platform project by the Ministry of Education, Culture, Sports, Science and Technology of Japan (A-20-UT-0335). This work was partially supported by a research grant from the Izumi Science and Technology Foundation.

## References

1 C. M. Niemeyer, *Angew. Chem., Int. Ed.*, 2001, **40**, 4128–4158.

2 G. Schmid, *Clusters and Colloids: From Theory to Applications*, John Wiley & Sons, 2008.

3 J. Wang, *Electroanalysis*, 2007, **19**, 769–776.

4 J. M. Pingarrón, P. Yañez-Sedeño and A. González-Cortés, *Electrochim. Acta*, 2008, **53**, 5848–5866.

5 S. Link and M. A. El-Sayed, *J. Phys. Chem. B*, 1999, **103**, 8410–8426.

6 Z. Zhong, S. Patskovskyy, P. Bouvrette, J. H. T. Luong and A. Gedanken, *J. Phys. Chem. B*, 2004, **108**, 4046–4052.

7 C. J. Murphy, T. K. Sau, A. M. Gole, C. J. Orendorff, J. Gao, L. Gou, S. E. Hunyadi and T. Li, *J. Phys. Chem. B*, 2005, **109**, 13857–13870.

8 E. Le Ru and P. Etchegoin, *Principles of Surface-Enhanced Raman Spectroscopy*, Elsevier, 2008.

9 R. Ferrando, J. Jellinek and R. L. Johnston, *Chem. Rev.*, 2008, **108**, 845–910.

10 M. B. Cortie and A. M. McDonagh, *Chem. Rev.*, 2011, **111**, 3713–3735.

11 H. You, S. Yang, B. Ding and H. Yang, *Chem. Soc. Rev.*, 2013, **42**, 2880–2904.

12 F. Wang, K. Kusada, D. Wu, T. Yamamoto, T. Toriyama, S. Matsumura, Y. Nanba, M. Koyama and H. Kitagawa, *Angew. Chem., Int. Ed.*, 2018, **57**, 4505–4509.

13 G. De and C. N. R. Rao, *J. Mater. Chem.*, 2005, **15**, 891–894.

14 D. Alloyeau, C. Ricolleau, C. Mottet, T. Oikawa, C. Langlois, Y. Le Bouar, N. Braidy and A. Loiseau, *Nat. Mater.*, 2009, **8**, 940–946.

15 D. A. Slanac, W. G. Hardin, K. P. Johnston and K. J. Stevenson, *J. Am. Chem. Soc.*, 2012, **134**, 9812–9819.

16 P. Buchwalter, J. Rosé and P. Braunstein, *Chem. Rev.*, 2015, **115**, 28–126.

17 S. Thota, Y. Wang and J. Zhao, *Mater. Chem. Front.*, 2018, **2**, 1074–1089.

18 S. Xiao, W. Hu, W. Luo, Y. Wu, X. Li and H. Deng, *Eur. Phys. J. B*, 2006, **54**, 479–484.

19 T. Nakamura, Y. Mochidzuki and S. Sato, *J. Mater. Res.*, 2008, **23**, 968–974.

20 K. Okazaki, T. Kiyama, K. Hirahara, N. Tanaka, S. Kuwabata and T. Torimoto, *Chem. Commun.*, 2008, 691–693.

21 H. Randhawa, *Thin Solid Films*, 1988, **167**, 175–186.

22 M. Sadakiyo, M. Heima, T. Yamamoto, S. Matsumura, M. Matsuura, S. Sugimoto, K. Kato, M. Takata and M. Yamauchi, *Dalton Trans.*, 2015, **44**, 15764–15768.

23 L. Piccolo, S. Nassreddine, M. Aouine, C. Ulhaq and C. Geantet, *J. Catal.*, 2012, **292**, 173–180.

24 A. Habrioux, W. Vogel, M. Guinel, L. Guetaz, K. Servat, B. Kokoh and N. Alonso-Vante, *Phys. Chem. Chem. Phys.*, 2009, **11**, 3573–3579.

25 S. Link, Z. L. Wang and M. A. El-Sayed, *J. Phys. Chem. B*, 1999, **103**, 3529–3533.

26 L. Usón, V. Sebastian, A. Mayoral, J. L. Hueso, A. Eguizabal, M. Arruebo and J. Santamaria, *Nanoscale*, 2015, **7**, 10152–10161.

27 T. Morita, T. Suzuki, Y. Itoh, T. Konishi, C. Haneishi, N. Sonoda, T. Itoh, H. Masu, T. Okajima, H. Setoyama and N. Uehara, *Cryst. Growth Des.*, 2019, **19**, 6199–6206.

28 D. L. Andrews, T. Nann and R. H. Lipson, *Comprehensive Nanoscience and Nanotechnology*, Academic Press, 2019.

29 S.-H. Jeon, P. Xu, B. Zhang, N. H. Mack, H. Tsai, L. Y. Chiang and H.-L. Wang, *J. Mater. Chem.*, 2011, **21**, 2550–2554.

30 J. Qiao, H. Ding, Q. Liu, R. Zhang and L. Qi, *Anal. Chem.*, 2017, **89**, 2080–2085.

31 N. Uehara, M. Fujita and T. Shimizu, *J. Colloid Interface Sci.*, 2011, **359**, 142–147.

32 J. A. Blackman, *Metallic Nanoparticles. In Handbook of Metal Physics*, ed. P. Misra, Elsevier, Amsterdam, The Netherlands, 2009, vol. **5**.

33 M. Zhou, C. Li and J. Fang, *Chem. Rev.*, 2021, **121**, 736–795.

34 K. Kusada, H. Kobayashi, R. Ikeda, Y. Kubota, M. Takata, S. Toh, T. Yamamoto, S. Matsumura, N. Sumi, K. Sato, K. Nagaoka and H. Kitagawa, *J. Am. Chem. Soc.*, 2014, **136**, 1864–1871.

35 A. Yang, O. Sakata, K. Kusada, T. Yayama, H. Yoshikawa, T. Ishimoto, M. Koyama, H. Kobayashi and H. Kitagawa, *Appl. Phys. Lett.*, 2014, **105**, 153109.

36 A. N. Mansour, J. W. Cook Jr and D. E. Sayers, *J. Phys. Chem.*, 1984, **88**, 2330–2334.

37 D. Friebel, D. J. Miller, C. P. O'Grady, T. Anniyev, J. Bargar, U. Bergmann, H. Ogasawara, K. T. Wikfeldt, L. G. M. Pettersson and A. Nilsson, *Phys. Chem. Chem. Phys.*, 2011, **13**, 262–266.

38 D. Wang, X. Cui, Q. Xiao, Y. Hu, Z. Wang, Y. M. Yiu and T. K. Sham, *AIP Adv.*, 2018, **8**, 065210.

39 T. K. Sham, M. J. Ward, M. W. Murphy, L. J. Liu and W. Q. Han, *J. Phys.: Conf. Ser.*, 2013, **430**, 012018.

40 M. J. Piotrowski, P. Piquini and J. L. F. Da Silva, *J. Phys. Chem. C*, 2012, **116**, 18432–18439.

41 T. Morita, K. Kurihara, O. Yoshida, H. Imamura, Y. Hatakeyama, K. Nishikawa and N. Uehara, *J. Phys. Chem. C*, 2013, **117**, 13602–13608.

42 K. Aika, L. L. Ban, I. Okura, S. Namba and J. Turkevich, *J. Res. Inst. Catal., Hokkaido Univ.*, 1976, **24**, 54–64.

43 T. Saitoh, Y. Yoshida, T. Matsudo, S. Fujiwara, A. Dobashi, K. Iwaki, Y. Suzuki and C. Matsubara, *Anal. Chem.*, 1999, **71**, 4506–4512.

44 T. Okajima and R. Ohtani, *DLS Proc.*, 2011, **1**, e141.

45 B. Ravel and M. Newville, *J. Synchrotron Radiat.*, 2005, **12**, 537–541.

46 M. Nomura and K. Koyama, *KEK Rep.*, 1996, **95–15**, 1–21.

47 P. Blaha, K. Schwarz, G. K. H. Madsen, D. Kvasnicka, J. Luitz, R. Laskowski, F. Tran and L. D. Marks, *WIEN2k, An Augmented Plane Wave + Local Orbitals Program for Calculating Crystal Properties* (Karlheinz Schwarz, Vienna University of Technology, Austria), 2018. ISBN 3-9501031-1-2.

48 C. Ambrosch-Draxl and J. O. Sofo, *Comput. Phys. Commun.*, 2006, **175**, 1–14.

49 A. H. MacDonald, W. E. Picket and D. D. Koelling, *J. Phys. C: Solid State Phys.*, 1980, **13**, 2675–2683.

50 J. P. Perdew, K. Burke and M. Ernzerhof, *Phys. Rev. Lett.*, 1996, **77**, 3865–3868.

51 N. T. K. Thanh, N. Maclean and S. Mahiddine, *Chem. Rev.*, 2014, **114**, 7610–7630.

52 H. Okamoto and T. B. Massalski, *Bull. Alloy Phase Diagrams*, 1985, **6**, 46–56.

53 V. Petkov, B. N. Wanjala, R. Loukrakpam, J. Luo, L. Yang, C. J. Zhong and S. Shastri, *Nano Lett.*, 2012, **12**, 4289–4299.

54 H. B. Liu, U. Pal and J. A. Ascencio, *J. Phys. Chem. C*, 2008, **112**, 19173–19177.

55 H. Sato and F. Hirata, *J. Chem. Phys.*, 1999, **111**, 8545–8555.

56 N. Yoshida, R. Ishizuka, H. Sato and F. Hirata, *J. Phys. Chem. B*, 2006, **110**, 8451–8458.

57 T. Ishimoto and M. Koyama, *J. Phys. Chem. Lett.*, 2016, 7(5), 736–740.

58 M. Harada and E. Katagiri, *Langmuir*, 2010, **26**, 17896–17905.